Proceedings of 2004 Korea-Japan Joint Seminar
on Particle Image Velocimetry
POSTECH, Korea, Dec. 9 - 10

Development of Zonal-Embedded-Grid Method for a Polar Coordinate System and Application to the Spin-up Flow within a Semi-Circular Cylinder

Yong Kweon SUH and Chang-Ho YEO

Department of Mechanical Engineering,
Dong-A University, Busan 604-714, Korea
yksuh@daunet.donga.ac.kr

Abstract: A zonal embedded grid technique has been developed for computation of the two-dimensional Navier-Stokes equations with cylindrical coordinates. The fundamental idea of the zonal embedded grid technique is that the number of azimuthal grids can be made small near the origin of the coordinates so that the grid size is more uniformly distributed over the domain than with the conventional regular-grid system. The code developed using this technique combined with the explicit, finite-volume method was then applied to calculation of the spin-up flows within a semi-circular cylinder. It was shown that the numerical results were in good agreement with the experimental results both qualitatively and quantitatively.

Keywords: Zonal embedded grid, Cylindrical coordinates, Explicit method, Spin-up flows, Semi-circular boundary

1. Introduction

Problems of fluid flow bounded by circular geometry are ubiquitous in engineering applications. For instance, a circular pipe becomes a first choice when we consider conveying gas or liquid from one place to another, and it is more natural to use a circular container, not a rectangular box, in designing a mixer in a chemical process.

In such geometry use of the cylindrical coordinate system, if possible, is the most relevant and desirable in the formulation and discretization of the Navier-Stokes equations in numerical simulations. Then, as a specific tool one may suggest employing a spectral method of some kind because the problem is periodic in the azimuthal direction, e.g. Verkley(1997), Lopez et. al(1998, 2002). However, the spectral method has a serious drawback associated with the Gibbs phenomenon for the case in which the first or second derivative of the flow field tends to be spatially discontinuous, which is not exceptional for high-Reynolds number flows.

Use of finite difference or finite volume method with the cylindrical coordinates (Verzicco and Orlandi, 1996, Fukagata and Kasagi, 2002) also reveals a fundamental problem when the regular grid system is employed as shown in Fig. 1(a). As is well known, under the regular grid system extremely small time steps must be taken for the sake of numerical stability, when an explicit method is employed, because the grid spacing in the azimuthal direction is proportional to the radial distance from the origin, and therefore the grid spacing at the center is usually some ten or hundred times smaller than that at the outer boundary. One remedy to overcome such restriction in the time step is to use an implicit method at least in the azimuthal direction as suggested by Akselvoll and Moin(1996). The implicit (or semi-implicit) method is indeed preferable in that a larger time step can be taken without causing the numerical instability. On the other hand,

however, the recent development of the parallel-computation technology makes the computational fluid dynamicists revisit the explicit method, because it is intrinsically more suitable for the parallel computation especially for the domain-decomposition method(Giraud and Manzini, 1996, Lomax et. al, 2001, Lin et. al, 2003). In addition, the programming is simple and flexible with the explicit method.

In this regard we propose to use the zonal embedded grid system shown in Fig. 1(b) rather than the simple regular grid system, Fig. 1(a), for the computation of fluid flow using an explicit method within a domain surrounded by a wall of circular geometry. With zonal embedded grids, we can control the azimuthal grid spacing independent of the radial distance from the origin, and thus the time step can be made significantly larger than that with the regular grids. In particular, it may be useful when an increased resolution in the azimuthal direction is required near the wall of a circular pipe in order to catch small vortical structures of turbulent flows at high Reynolds numbers. In this case, the azimuthal grid spacing near the wall can be set arbitrarily small while that near the pipe center is kept still large so that the critical time step occurs not at the center but near the wall itself, which is a clear indication of flexibility in the grid design.

Use of zonal embedded grids in computational fluid dynamics is not new. Kravchenko, et. al(1996) introduced zonal embedded grids in a numerical study on the turbulent flow above a flat plate. However no studies have been found in the literature that employed the zonal embedded grid system in solving a fluid flow problem with the cylindrical coordinates.

2. Formulation of the Governing Equations

To illustrate the development of the zonal embedded grid method, we select a specific flow problem. Consider an incompressible fluid of density ρ and kinematic viscosity ν within a semicircular container of radius R. The container being initially at a solid body rotation with the angular velocity $\Omega - \Delta\Omega$ is subjected at the time $t = 0$ to an increase of the angular velocity as much as $\Delta\Omega$ so that the final velocity becomes Ω. It is well known that when the ratio $\Delta\Omega/\Omega$, called the Rossby number and denoted as ε in this paper, is small enough the axial flow (flow along the axis of rotation) is inhibited and the flow tends to be basically two-dimensional(Greenspan, 1968). We are interested in the numerical simulation of the spin-up flows generated during the speed-up process by using the zonal embedded grid system. By taking R as the reference length, $R\Delta\Omega$ as the reference velocity, and $1/\Delta\Omega$ as the reference time, we can write the governing equations, in terms of the cylindrical coordinates, in a dimensionless form as follows.

$$\frac{\partial ru}{r\partial r} + \frac{\partial v}{r\partial \theta} = w, \tag{1}$$

$$\frac{\partial u}{\partial t} + \frac{\partial ru^2}{r\partial r} + \frac{\partial uv}{r\partial \theta} - \frac{v^2}{r} = -\frac{\partial p}{\partial r} + \frac{1}{\mathrm{Re}}\left[\frac{\partial}{r\partial r}\left(\frac{r\partial u}{\partial r}\right) + \frac{\partial^2 u}{r^2\partial\theta^2} - \frac{u}{r^2} - \frac{2}{r^2}\frac{\partial v}{\partial\theta}\right] + f \tag{2a}$$

$$\frac{\partial v}{\partial t} + \frac{\partial ruv}{r\partial r} + \frac{\partial v^2}{r\partial \theta} + \frac{uv}{r} = -\frac{\partial p}{r\partial\theta} + \frac{1}{\mathrm{Re}}\left[\frac{\partial}{r\partial r}\left(\frac{r\partial v}{\partial r}\right) + \frac{\partial^2 v}{r^2\partial\theta^2} - \frac{v}{r^2} + \frac{2}{r^2}\frac{\partial u}{\partial\theta}\right] + g \tag{2b}$$

where all the variables are dimensionless; t is the time, r and θ the radial and azimuthal coordinates respectively, u and v the velocity components along each direction, and p the pressure. The mass-source term w and the body-force terms f and g on the right-hand sides of the above equations are

$$w = W_E / h, \tag{3a}$$

$$f = 2(q(t) + 1/\varepsilon)v + uW_E / h, \tag{3b}$$

$$g = -2(q(t) + 1/\varepsilon)u + vW_E / h - rq'(t), \tag{3c}$$

where the Ekman-pumping velocity W_E is given by the linear Ekman-pumping law(Suh and Choi, 2002)

$$W_E = \frac{\sqrt{\varepsilon/\mathrm{Re}}}{2}\varsigma, \tag{4}$$

where the vorticity ς is determined by

$$\varsigma = \frac{1}{r}\left(\frac{\partial rv}{\partial r} - \frac{\partial u}{\partial \theta}\right) \tag{5}$$

and h is the dimensionless liquid depth in a quiescent state. This pumping velocity brings the non-zero mass source w in (1), which tends to be uniformly distributed over the liquid column at low Rossby numbers, in such a way that the two-dimensional assumption be valid (e.g. Suh and Choi, 2002). The function $q(t)$ controls the speed-up mode, and for a smooth operation we employ the harmonic function:

$$q = \begin{cases} -(1+\cos\omega t)/2 & \text{for } 0 \le t \le t_s \\ 0 & \text{for } t \ge t_s \end{cases}. \tag{6}$$

The speed-up time t_s is related to ω by $t_s = \pi/\omega$. The Reynolds number is defined as

$$\mathrm{Re} = \frac{R^2 \Delta\Omega}{\nu}.$$

3. Zonal Embedded Grid System and Numerical Methods

To construct a zonal embedded grid system, the entire domain is first divided into several sub-domains or zones by concentric circles. Figure 1(b) shows the case with four zones. In each zone the grids are built in the same way as the regular grids are made. However, the number of grids in the azimuthal direction differs from one zone to another, and following the purpose of this study, we increase the number of azimuthal grids in the outer zone. The simplest way to do this is to double the number of grids each time one crosses the zones radially outward. Figure 1(b) is a typical example in that it starts from 16 grid lines in the innermost zone and 32 lines in the next, progressing to 128 lines in the outermost zone. To keep a constant azimuthal grid-spacing at the outer end position of each zone, we need to double the radial size of each zone as one crosses the zones outward, except for the second zone as illustrated below.

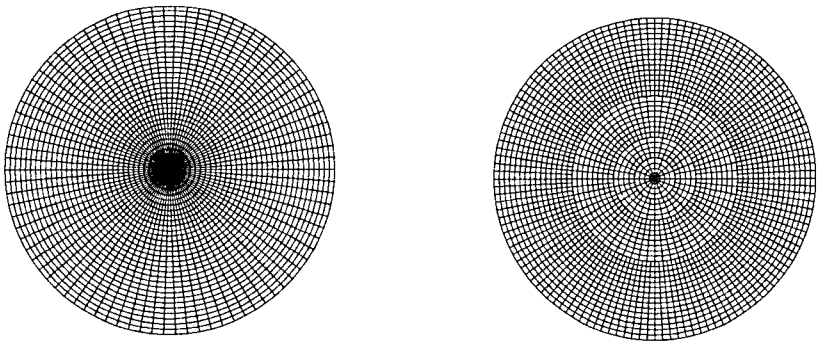

(a) regular grids (b) zonal embedded grids

Fig. 1. Regular and zonal embedded grids for the domain within a circle. $I \times J = 32 \times 86$ for the regular grids and $M = 4$, $I_0 = 4$, $J_0 = 16$ ($I \times \overline{J} = 32 \times 86$) for the zonal embedded grids.

Suppose we have M zones. Then I_m, the number of radial grids, and J_m, the number of azimuthal grids, at the m'th zone are given by

$$I_m = \begin{cases} I_0 & \text{for } m = 1 \\ 2^{m-2} I_0 & \text{for } 2 \le m \le M \end{cases}, \tag{7a}$$

$$J_m = 2^{m-1} J_0 \quad (m = 1, 2, \ldots, M), \tag{7b}$$

where I_0 and J_0 are the number of grids in the first zone. The reason of taking the same I_m for

the first and second zones is related to the implementation of the extrapolation scheme $\partial^3\phi/\partial r^3 = 0$ in evaluation of a flow variable ϕ near the center point. In order to use only the first zone's variables in this extrapolation, so that the algorithm becomes simple, at least four radial grids must be established in the first zone, $I_0 \geq 4$. For instance, with $M = 4$, $I_0 = 4$, if we use the formula $I_m = 2^{m-1} I_0$ $(1 \leq m \leq M)$ instead of (7a), then $I_m = 4$, 8, 16, 32 and the total number of radial grids becomes $I = 60$. On the other hand, if we use (7a), then $I_m = 4$, 4, 8, 16 and we have $I = 32$. Thus Equation (7a) allows for implementation of a simple extrapolation scheme near the center point at a lower I. Parameters I_0 and J_0 together with M control the overall grid spacings. The averaged number of the azimuthal grids, $\bar{J}$, is given by

$$\bar{J} = \frac{1}{I} \sum_{m=1}^{M} I_m J_m$$

Figure 1(b) is made with $M = 4$, $I_0 = 4$ and $J_0 = 16$, which gives the total number of radial grids within the entire domain, $I = 32$, the number of azimuthal grids in the outermost zone, $J = 128$, and the averaged number of azimuthal grids, $\bar{J} = 86$.

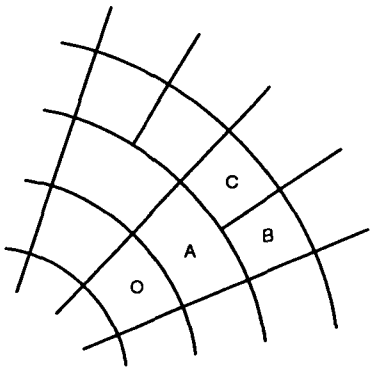

Fig. 2. Four types of cells in the zonal embedded grid system.

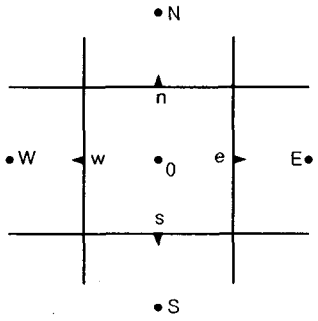

(a) regular p-cell of "O" type

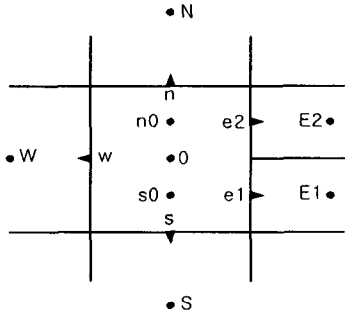

(b) special p-cell of "A" type

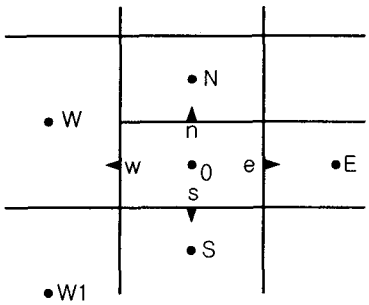

(c) special p-cell of "B" type

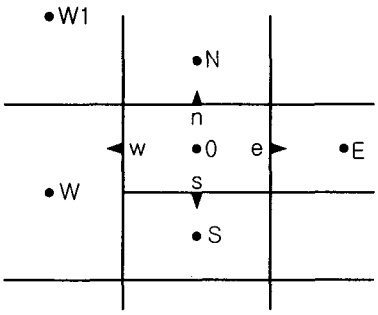

(d) special p-cell of "C" type

Fig. 3. Four types of p-cells with various symbols to be used in discretization.

Associated with the allocation of pressure and velocity components in each cell, we employ the staggered-grid method; the pressure is defined at the center of the p-cell, and the velocity component at the mid point of each line normal to the component surrounding the p-cell. There are two kinds of p-cells; one is a regular cell composed of four edges(cells marked "O", "B", and "C" in Fig. 2) and the other is a special cell composed of five edges (marked "A" in Fig. 2).

The continuity equation (1) is first integrated over the regular p-cell shown in Fig. 3(a). The result is

$$u_e\Delta s_e - u_w\Delta s_w + v_n\Delta r - v_s\Delta r = \Delta s_0\Delta r\, w_0^o, \tag{8}$$

where Δr and Δs ($=r\Delta\theta$) are the radial and azimuthal grid spacings respectively and w_0^o represents the value of w at the cell's center point "0" given at the previous time step. The superscript "o" indicates that the variable is known and evaluated at the previous time step. Notice that, for the spin-up flows, the right-hand side also contains the unknown velocity components u and v. Treating these variables really unknown, like the other velocity components on the left-hand side of (8), inevitably results in a much complex pressure-equation. Therefore we treat these terms explicitly. The underlying principle for the relevance of treating the right-hand side of (8) known comes from the fact that at high Reynolds numbers the magnitude of w is in general much smaller than that of u or v. The momentum equations (2a) and (2b) are then integrated over the regular u- and v-cells respectively to give

$$u_e = u_e^o + \Delta\tau\left(F_e - \frac{p_E - p_0}{\Delta r}\right),\quad u_w = u_w^o + \Delta\tau\left(F_w - \frac{p_0 - p_W}{\Delta r}\right), \tag{9a}$$

$$v_n = v_n^o + \Delta\tau\left(G_n - \frac{p_N - p_0}{\Delta s_0}\right),\quad v_s = v_s^o + \Delta\tau\left(G_s - \frac{p_0 - p_S}{\Delta s_0}\right), \tag{9b}$$

where F and G denote the momentum fluxes containing the convection, diffusion and source terms. The time step $\Delta\tau$ takes Δt or $\Delta t/2$ depending on the stage number within one step of the 4th-order Runge-Kutta method. The subscripts in (9a) and (9b) are still based on the p-cell. Substituting these results into the discretized continuity equation (8) gives us the pressure equation reading:

$$a_w p_W + a_s p_S + a_0 p_0 + a_e p_E + a_n p_N = b, \tag{10}$$

where b contains w_0^{oo}, the value of w_0 at the previous-previous time step, as well as w_0^o, the value of w_0 at the previous time step. Here too, the term $(w_0 - w_0^o)/\Delta t$ on the right-hand side of the equation for b has been replaced by $(w_0^o - w_0^{oo})/\Delta t$ to avoid complexity; in fact the former corresponds to a disctretized form of $\partial w/\partial t$. An easy way of implementing the impermeable condition at the walls is to set both the corresponding coefficient a and flux F or G zero at the edge of the cell contacting each wall.

For the special p-cell of "A" type shown in Fig. 3(b), the continuity equation takes the form

$$(u_{e1} + u_{e2})\Delta s_e - u_w\Delta s_w + v_n\Delta r - v_s\Delta r = \Delta s_0\Delta r\, w_0^o, \tag{11}$$

where the formula for u_{e1} and u_{e2} now contain p_S and p_N;

$$u_{e1} = u_{e1}^o + \Delta\tau\left(F_{e1} - \frac{p_{E1} - p_0}{\Delta r}\right) - \Delta\tau\frac{p_0 - p_S}{4\Delta r}, \tag{12a}$$

$$u_{e2} = u_{e2}^o + \Delta\tau\left(F_{e2} - \frac{p_{E2} - p_0}{\Delta r}\right) - \Delta\tau\frac{p_0 - p_N}{4\Delta r}. \tag{12b}$$

The last term on the right-hand side of each of these equations comes from discretization of $\partial p/\partial r$ at the point "e1" or "e2" while keeping the second-order accuracy. For instance at the point "e1" we have $\partial p/\partial r = (p_{E1} - p_{s0})/\Delta r$ and a linear interpolation gives $p_{s0} = (3p_0 + p_S)/4$, which results in

$\partial p/\partial r = (p_{E1} - p_0)/\Delta r + (p_0 - p_S)/4\Delta r$. The first term on the right-hand side of this equation is included in the bracket on the right-hand side of (12a). It can be shown that the matrix of the discretized pressure equation system to be given by substituting (12a) and (12b) into the continuity equation keeps the symmetry property. Now, substituting (12a) and (12b) together with the formula for u_w, v_n and v_s into (11) yields

$$a_w p_W + a_s p_S + a_0 p_0 + a_{e1} p_{E1} + a_{e2} p_{E2} + a_n p_N = b .$$

Special attention must be given to the cells adjacent to the walls. The coefficient a at the edge contacting the wall must be set at zero. It is also required to set F at zero at the edge contacting the wall at $r = 1$ or at the origin $r = 0$. However, when the cell is contacting the flat wall at $\theta = 0$ or at $\theta = \pi$ for the case of the semi-circular problem, the variable G should not be set at zero, and further the variable b takes a different form depending on whether the cell faces the wall at the "s" edge ($\theta = 0$) or it faces the wall at the "n" edge($\theta = \pi$).

For the p-cell of "B" type shown in Fig. 3(c), the discretized continuity equation takes the same form as (8). The formula for u_e, v_n and v_s are also the same as the corresponding ones in (9a) and (9b). Substituting these into (8), we get the result of (10) and all the coefficients are also the same as the corresponding ones. For the "B" type cell too, we must pay a special attention to the evaluation of coefficients near the walls.

For the p-cell of "C" type shown in Fig. 3(d), we can follow a very similar procedure as the case for the "B" type cell described above. Special attention must be given to evaluating w_0 in terms of the velocity components u and v.

In discretization of the momentum flux F and G appearing in the pressure equations, two kinds of algorithms for the azimuthal derivatives are used. The first kind is the second-order algorithm

$$\left(\frac{\delta\phi}{\delta\theta}\right)_0 = \frac{\phi_+ - \phi_-}{\Delta\theta}, \tag{13a}$$

and the second is the forth-order algorithm

$$\left(\frac{\delta\phi}{\delta\theta}\right)_0 = \frac{27(\phi_+ - \phi_-) + \phi_{++} - \phi_{--}}{24\Delta\theta}, \tag{13b}$$

where ϕ_+, ϕ_+, ϕ_{++} and ϕ_{--} denote the value of the variable ϕ at the points apart from the point "0" as much as $\Delta\theta/2$, $-\Delta\theta/2$, $3\Delta\theta/2$ and $-3\Delta\theta/2$ respectively, in the θ-direction. In evaluating the ϕ-values at the points where the variable is not defined, we used two kinds of interpolation algorithms:

$$\phi_0 = \frac{\phi_+ + \phi_-}{2} \tag{14a}$$

as the second-order and

$$\phi_0 = \frac{9(\phi_+ + \phi_-) - (\phi_{++} + \phi_{--})}{16} \tag{14b}$$

as the forth-order formula. It was found that application of the second-order formula brings a significant error in the numerical results when the flow near the origin of the coordinate system is characterized basically as a uniform flow. For instance, when the flow near the origin is uniform with the speed U and directed along the x-direction, its velocity components can be described asymptotically as $u = U\cos\theta$, $v = -U\sin\theta$ and therefore the variation of these variables are significant because $\Delta\theta$ is in general large near the origin. Since making $\Delta\theta$ large near the origin corresponds in practice to the fundamental reason for the introduction of the zonal embedded-grid method, employing higher-order algorithms such as (13b) and (14b) instead of (13a) and (14a) is very important for successful applications. When the flow is purely radial or azimuthal, we have $\delta\phi/\delta\theta = 0$, and there is no difference between the second- and forth-order algorithms.

4. Numerical Results and Discussions

The numerical algorithms developed in this study were tested for spin-up flows inside a semi-circular boundary. In contrast to the spin-up within a full circular container, due to the existence of corners inside the domain, this configuration generates a boundary-layer separation from the solid walls. The separated flow then undergoes a vortex roll-up, vortex growth, and vortex merging. Such dynamical behavior is most typical in the complex fluid flows and thus the spin-up flow inside a semi-circular container is thought to be suitable in verifying the code for a general purpose. This kind of flow was first studied experimentally by van Heijst(1989) at the Reynolds number 1.6×10^5 and for various liquid depths. The three-dimensional numerical computation of this flow was then conducted by Andersson et al.(1992). However their numerical results are not in good agreement with the

Table 1. Effect of grid system (M, I_0, J_0) on the limit of the time step $\Delta t_{\lim}$ for a spin-up flow inside a semi-circular cylinder; $\mathrm{Re}=5000$, $\varepsilon=1$, $h=1$, $\omega=10$.

grid system ($I\times J$; M, I_0, J_0)	$\Delta t_{\lim}$
64×256 ; 5, 4, 16	0.012
64×256 ; 4, 8, 32	0.0053
64×256 ; 3, 16, 64	0.0017

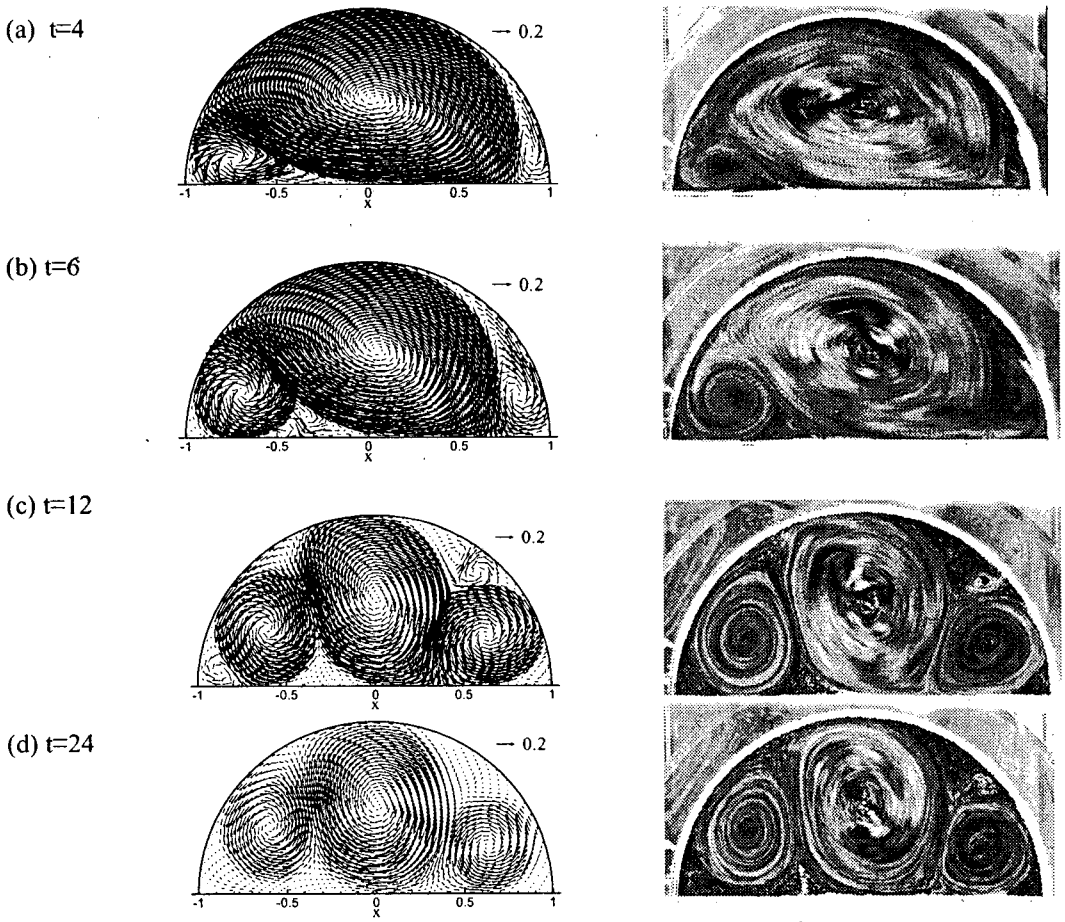

Fig. 4. Development of the velocity-vector field obtained numerically (left-hand side) for $\mathrm{Re}=5{,}000$, $\varepsilon=0.5$, $h=1$ and $\omega=6.54$ with grids $(M, I_0, J_0)=(5,4,16)$ and development of the pathlines obtained from a flow-visualization experiment with acrylic powders floated on tap water.

experimental results. For instance, the experimentally observed phenomena such as vortex merging were not observed in the numerical experiment. The fundamental reason for such a discrepancy seems to be the low resolution of the grid system for such a high Reynolds-number flow. The numerical results presented in this subsection are obtained from the code with zonal embedded grids employing the non-conservative $O(\Delta\theta^4)$-algorithm with the viscous terms in the original form.

First of all, the numerical stability was tested to this flow. Table 1 shows the results for $\mathrm{Re} = 5{,}000$ and $I \times J = 64 \times 256$, which are fixed, and for three choices of (M, I_0, J_0). This result suggests that when decreasing M and increasing I_0 and J_0 simultaneously, we should make the time step smaller for a stable computation. Since increase of J_0 results in the decrease of the azimuthal-grid size near the origin, it again implies that the numerical stability is simply decided by the azimuthal-grid size at the origin, which is the smallest over the domain.

Figure 4 shows the development of the velocity vectors, at $\mathrm{Re} = 5000$ and $\varepsilon = 0.5$, given from the numerical solution in comparison with the experimental pathlines. In this flow, the speed-up of the container ends at $t = 0.48$ and its speed is maintained at this value thereafter. The background rotation is counterclockwise. Since most of the pathlines do not intersect with each other, they can be considered to be very close to streamlines. First of all, it is remarkable to see that the numerical solution exactly reproduces the experimentally observed one. At the very beginning of the development the flow is occupied by a large anticyclonic cell (to be referred to as 'primary' vortex hereafter), which is inviscid with a uniform vorticity $\varsigma = -2$ except for the thin boundary layers adjacent to the walls. Due to the existence of two corners, however, this vortex brings forth boundary-layer separations from the surrounding walls and the separated layers roll up to form a cyclonic vortex near each corner (Fig. 4a). The corner vortices (to be referred to as 'secondary' vortices hereafter) then grow to be almost comparable in size with the primary vortex (Figs. 4c, d, e). During this development, the primary vortex imparts its material to the secondary vortices via the roll-up process discussed above and shrinks finally to a size approximately one third of the domain. At the final stage (Figs. 4d, e) the secondary vortex at the left-hand side is slightly shifted toward the circular boundary, but it stays there all the way until the flow vanishes completely.

Figure 5 shows the distribution of the azimuthal velocity component along the line $\theta = \pi/2$ obtained numerically for the same parameter values as Fig. 4 in comparison with the experimental results measured by the PIV method. Here the PIV results are obtained by using the MQD-PIV method developed by Suh(2003). Two results are in good agreement with each other except near the boundary, where due to a high velocity-gradient it is generally difficult to measure the velocity accurately. Overall, the velocity decreases in time due to the damping caused by the pumping/suction of the fluid material from the Ekman boundary-layer on the bottom wall of the container; such pumping/suction is treated by the Ekman pumping velocity W_E, Eq. (4).

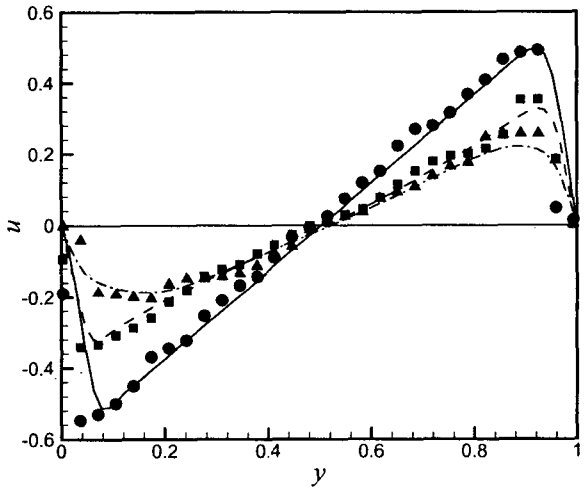

Fig. 5. u-velocity profiles along the y-axis at $t = 6$ (solid line and circles), $t = 12$ (dashed line and squares) and $t = 12$ (dash-dot line and deltas) obtained numerically(lines) and experimentally(symbols) for the spin-up flow in a semi-circular boundary with the same parameter set as Fig. 4.

At higher Reynolds numbers and Rossby numbers, the flow pattern becomes more complex due to a lower damping effect. Figure 6 shows streamlines obtained numerically and pathlines given from the experiment for $\mathrm{Re}=10{,}000$ and $\varepsilon=1$. The experimental pathlines are considered to be approximately the same as the corresponding streamlines. Many small third vortices appear strong in the regions between the primary or secondary vortices and corners or walls, where the flow was almost stagnant at lower Reynolds numbers(Fig. 4). Here, the third vortex near the left-hand side corner and the primary vortex enforce the satellite vortex travel along the circular boundary (Figs. 6d and e) toward the right-hand side of the domain. After the transposition, the vortex is expected to merge with the secondary vortex situated near the right-hand corner. Overall, the numerical and experimental results are in good agreement with each other except in Fig. 6(e), where the numerical results reveal a faster movement of the satellite vortex than the experiment.

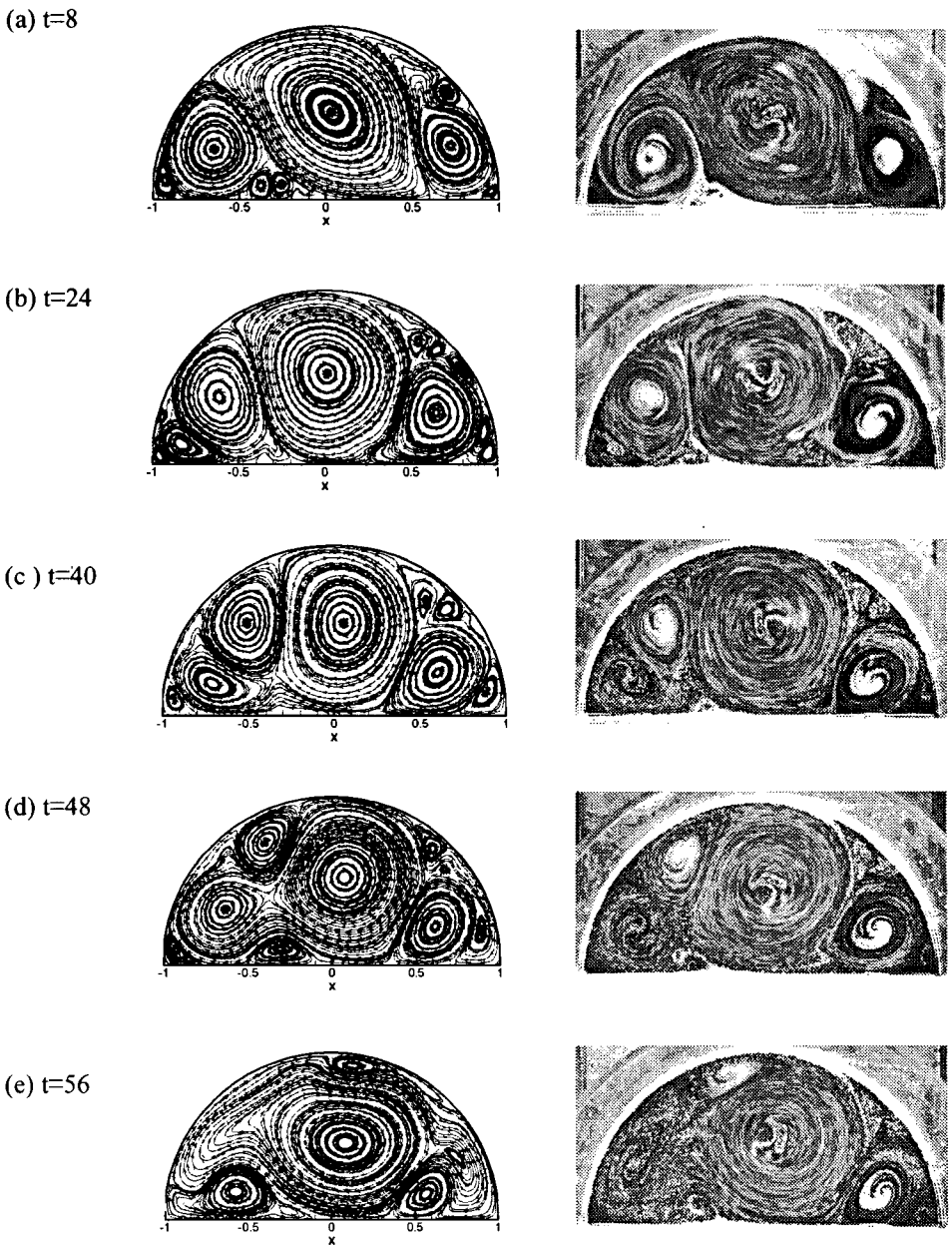

Fig. 6. Development of the streamlines obtained numerically (left-hand side) for $\mathrm{Re}=10{,}000$, $\varepsilon=1$, $h=1$ and $\omega=6.54$ with grids $(M, I_0, J_0)=(5,8,32)$ in comparison with the pathlines obtained from a flow-visualization experiment (right-hand side).

5. Conclusions

In this study a zonal-embedded-grid technique has been proposed for numerical simulation of flows within a circular boundary with cylindrical coordinates. The benefit of this method is that even with the explicit method, it allows a time step far larger than the conventional regular-grid system. In discretization of the azimuthal derivatives and evaluation of variables at undefined points, this method requires employing higher-order algorithms such as forth-order to establish numerical accuracy, because the number of grids along the azimuthal direction is relatively small near the origin of the coordinates. The developed code was applied to spin-up flows within a semi-circle. At relatively low Reynolds and Rossby numbers ($\mathrm{Re} = 5{,}000$, $\varepsilon = 0.5$), the spin-up flow organized by a three-cell structure was well predicted by the two-dimensional numerical simulation. At high Reynolds and Rossby numbers ($\mathrm{Re} = 10{,}000$, $\varepsilon = 1$), the flow field was occupied by many smaller vortices, and in this case too the numerical results well predict the overall vertical dynamics including the peculiar phenomenon observed in the experiment, i.e. transposition of the satellite vortex from one corner to the other.

ACKNOWLEDGEMENT

This work has been supported by the Korea Research Foundation (KRF-2002-D00080). We appreciate Professor M. Duffy for reading the manuscript.

References

Akselvoll K, Moin P., "An efficient method for temporal integration of the Navier-Stokes equations in confined axisymmetric geometries," *J. Comput. Phys.* 1996; **125**: 454-463.

Andersson HI, Billdal JT, van Heijst GJF., "Spin-up in a semicircular cylinder," *Int. J. Num. Methods Fluids.* 1992; **15**: 503-524.

Fukagata K, Kasagi N., "Highly energy-conservative finite difference method for the cylindrical coordinate system," *J. Comput. Phys.* 2002; **181**: 478-498.

Giraud L, Manzini G., "Parallel implementations of 2D explicit Euler solvers," *J. Comput. Phys,* **1996; 123**: 111-118.

Greenspan HP., *The Theory of Rotating Fluids*; Cambridge University Press, Cambridge, UK, 1968.

Kravchenko AG, Moin P, Moser R., "Zonal embedded grids for numerical simulations of wall-bounded turbulent flows," *J. Comput. Phys.* 1996; **127**: 412-423.

Lin P, Guo Q, Chen X., "A fully explicit methods for incompressible flow computation," *Comput. Methods Appl. Mech. Engrg.* 2003; **192**: 2555-2564.

Lomax H, Pulliam TH, Zingg DW., *Fundamentals of Computational Fluid Dynamics*; Springer, 2001.

Lopez JK, Shen J., "An efficient spectral-projection method for the Navier-Stokes equations in cylindrical geometries. I. Axisymmetric cases," *J. Comput. Phys.* 1998; **139**: 308-326.

Lopez JK, Marques F, Shen J., "An efficient spectral-projection method for the Navier-Stokes equations in cylindrical geometries. II. Three-dimensional cases," *J. Comput. Phys.* 2002; **176**: 384-401.

Suh YK., "Multi-frame MQD-PIV," *KSME Int. J.* 2003; **17**: 1463-1473.

Suh YK, Choi YH., "Study on the spin-up of fluids in a rectangular container using Ekman pumping models," *J. Fluid Mech.* 2002; **458**: 103-132.

van Heijst GJF., "Spin-up phenomena in non-axisymmetric containers," *J. Fluid Mech.* 1989; **206**: 171-191.

Verkley WTM., "A spectral model for two-dimensional incompressible fluid flow in a circular basin. I. Mathematical formulation," *J. Comput. Phys.* 1997; **136**: 100-114.

Verkley WTM., "A spectral model for two-dimensional incompressible fluid flow in a circular basin. II. Numerical examples," *J. Comput. Phys.* 1997; **136**: 115-131.

Verzicco R, Orlandi P., "A finite-difference scheme for three-dimensional incompressible flows in cylindrical coordinates," *J. Comput. Phys.* 1996; **123**: 402-414.